Article

In Situ Study of the Activation Process of MOF-74 Using Three-Dimensional Electron Diffraction

Matthias Quintelier, Amirhossein Hajizadeh, Alexander Zintler, Bruna F. Gonçalves, Roberto Fernández de Luis, Leili Esrafili Dizaji, Christophe M. L. Vande Velde, Stefan Wuttke, and Joke Hadermann*

Read Online

ACCESS | Metrics & More | Article Recommendations | SI Supporting Information

ABSTRACT: Metal−organic framework (MOF)-74 is known for its effectiveness in selectively capturing carbon dioxide (CO_2). Especially the Zn and Cu versions of MOF-74 show high efficiency of this material for CO_2. However, the activation of this MOF, which is a crucial step for its utilization, is so far not well understood. Here, we are closing the knowledge gap by examining the activation using, for the first time in the MOF, three-dimensional electron diffraction (3DED) during *in situ* heating. The use of state-of-the-art direct electron detectors enables rapid acquisition and minimal exposure times, therefore minimizing beam damage to the very electron beam-sensitive MOF material. The activation process of Zn-MOF-74 and Cu-MOF-74 is systematically studied *in situ*, proving the creation of open metal sites. Differences in thermal stability between Zn-MOF-74 and Cu-MOF-74 are attributed to the strength of the metal−oxygen bonds and Jahn−Teller distortions. In the case of Zn-MOF-74, we observe previously unknown remaining electrostatic potentials inside the MOF pores, which indicate the presence of remaining atoms that might impede gas flow throughout the structure when using the MOF for absorption purposes. We believe our study exemplifies the significance of employing advanced characterization techniques to enhance our material understanding, which is a crucial step for unlocking the full potential of MOFs in various applications.
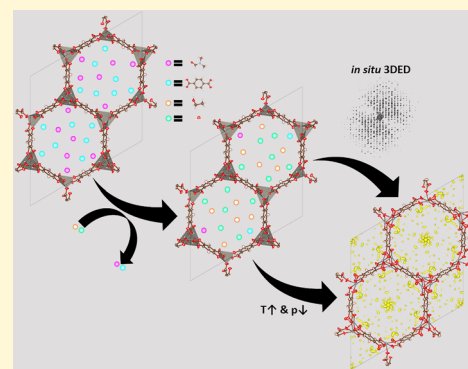
INTRODUCTION

Metal−organic frameworks (MOFs) represent a category of microporous materials characterized by large internal surface areas, structural control over the framework, and customizable framework functionalities.[1,2] Among the many applications of MOFs, an important one lies in their capacity to selectively absorb various gases, with particular significance attributed to carbon dioxide (CO_2) due to its pivotal role in global warming.[3−6] Many MOFs are capable of CO_2 absorption/desorption, but MOF-74 is an excellent candidate in this regard.[7−13] Here, the versatility that MOF-74 has to welcome plenty of divalent ions in its structure play an important role to tune its CO_2 adsorption capacity within the low-pressure regime.[14] Modulating the composition of metals such as Zn or Cu into MOF structures does not only alter the efficiency of MOF-74 for absorbing but also opens the room to transforming the CO_2 to CO, considering the significance of CO as a raw material for diverse hydrocarbon-based products.[15]

The potential impact and potential applications of MOF-74, however, go much further than only gas absorption and catalysis. This MOF can also be used for gas separation, gas storage, drug delivery, sensing, detection, and water purification, just to mention some of the most relevant application fields explored up to date.[16−19]

However, before any MOF can effectively absorb gases or can be used for any other application based on MOF-guest interactions, it must undergo an activation.[20,21] During MOF synthesis, solvents like *N,N*-dimethylformamide (DMF), water (H_2O), ethanol (EtOH), and unbound linkers tend to bind to the metal nodes, obstructing the MOF pores and rendering them inaccessible to gas molecules. Activation is a crucial procedure wherein these pores are emptied, and open metal sites are generated, enabling gas molecules to bind effectively. The activation procedure of some MOFs can be a challenging and multistage process including the exposure of the material to solvent exchange, vacuum, and/or heating to elevated temperatures. This is specially the case of MOF materials as MOF-74, containing open metal sites in their crystal structures. All in all, the full activation of MOF-74 needs to be performed without altering the crystallinity or the porosity of the framework.
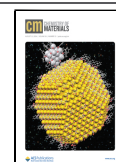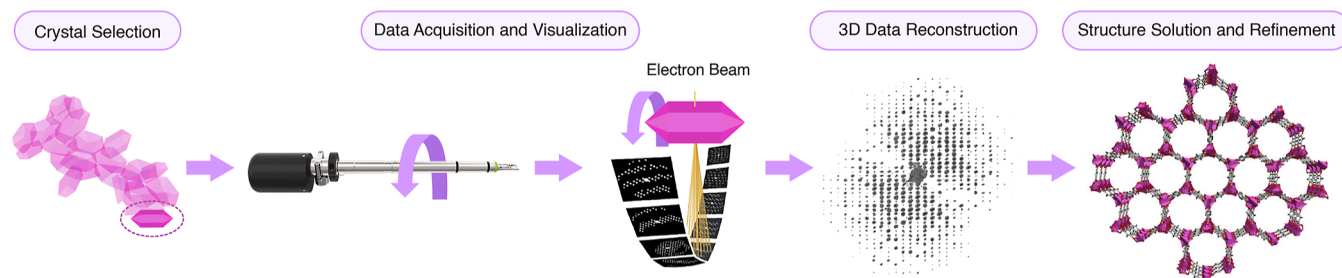
Figure 1. Schematic representation of the workflow of a three-dimensional electron diffraction experiment.

So far, MOF-74 activation has been exclusively investigated through ex situ analysis by powder X-ray diffraction (PXRD).[22−24] However, PXRD gives a limited view of MOFs when the materials are obtained with particle sizes within the nanoregime, or the long-range ordering of the samples is limited due to the high degree or disorder or defects in their structure.[25] The difficulties caused by small coherence lengths go beyond just widening PXRD peaks—they also involve complex data interpretation because of overlapping peaks. In the case of micron- and submicron-sized particles, the adoption of three-dimensional electron diffraction (3DED) emerges as an indispensable tool for a meticulous understanding of the activation process.

3DED is an emerging characterization technique conducted using a transmission electron microscope.[26−29] It utilizes electron diffraction patterns obtained at various sample tilt angles to reconstruct the three-dimensional reciprocal space, as depicted in Figure 1. The reconstructed space enables the determination and refinement of the crystal structure of the investigated material. Due to the electron-based nature of 3DED, which exhibits stronger sample interaction compared to traditional X-rays, the method allows the acquisition of single-crystal type data from submicron-sized samples. This is particularly beneficial for materials that cannot be synthesized as the large single crystals (on the order of >0.1 mm^{30}) required for neutron or single-crystal X-ray coherent scattering (SCXRD). Additionally, 3DED minimizes dynamical contributions, reducing the impact of electron beam multiple scattering, a common hindrance to structural refinement from electron diffraction data. 3DED has already been proven to be successful in detecting guest molecules in MOF and SOF channels.[31,32] Several experimental methods for 3DED exist, including stepwise acquisition, involving a gradual tilt of the sample with a diffraction pattern acquired at each step,[33] and continuous rotation electron diffraction (cRED),[34] where the sample undergoes a continuous tilt while diffraction patterns are continuously recorded (Figure 1). cRED, chosen for this study, facilitates rapid data acquisition, making it suitable for beam-sensitive materials like MOFs. Presently, 3DED can be used for all kinds of materials ranging from inorganics to proteins, and it can go as far as the determination of hydrogen positions in structures,[35,36] refinement of correlated disorder,[37] and quantification of phase percentages in multiphase materials.[38] Since 3DED is performed in a TEM, it can be seamlessly integrated with other microscopy techniques, such as scanning transmission electron microscopy (STEM) for imaging of the sample and energy-dispersive X-ray spectroscopy (EDX) for elemental analysis. The synergistic application of these techniques provides a comprehensive understanding of the investigated material.

In this work, we study the activation process of MOF-74, as an important proof-of-concept MOF example with impactful application potential, using for the first time in situ heating TEM on a MOF, a.o. with in situ 3DED. The application of TEM on MOFs generally suffers due to the materials sensitivity to the electron beam, causing structural damage. In addressing this beam damage, we reduced the total electron dose and increased the speed of the 3DED acquisition. To achieve this, we applied 3DED in continuous acquisition (cRED). using the CheeTah Direct Electron Detector (DED). The effectiveness of this mitigation strategy could be proven by consecutively taking unchanged structure analysis data sets. Our approach of examining the MOF activation process in-depth with 3DED, instead of the general applied PXRD analysis, allowed us to prove some of the activation steps while also revealing previously unknown features for this important stage in the application of this material.

■ EXPERIMENTAL SECTION

Synthesis of M-MOF-74 (M = CU, Zn). The synthesis protocol for Zn-MOF-74 was conducted following the methodology outlined by Liao et al.[39] In a screw cap vial, 1.021 g of zinc nitrate hexahydrate (3.43 mmol) was combined with 250 mg of 2,5-dihydroxybenzene-1,4-dicarboxylic acid (1.30 mmol), 50 mL of DMF, and 3 mL of water. The resulting mixture was stirred until complete dissolution of the starting materials, after which the tightly sealed solution was placed in a 100 °C oven for 24 h. Trigonal block crystals were obtained, and upon reaching room temperature, the mother solvent was decanted, and the remaining material underwent a triple wash with 30 mL of DMF.

The synthesis of Cu-MOF-74 was carried out following an adapted procedure as described by Flores et al.[59] Initially, 10 mmol (1.981 g) of 2,5-dihydroxyterephthalic acid was dissolved in 1370 mmol (100 g) of DMF under stirring at 60 °C. Separately, 20 mmol of copper acetate dihydrate was dissolved in another 1370 mmol (100 g) of DMF. The metal solution was then added dropwise to the organic linker solution under vigorous stirring at room temperature, resulting in the formation of a dark brown precipitate. The reaction mixture was stirred for 24 h at room temperature, followed by centrifugation, triple washing with DMF, triple washing with methanol, and finally drying at 120 °C overnight.

PXRD Structure Determination/Analysis. The structure of Zn-MOF-74 was determined by single-crystal X-ray diffraction by Yaghi et al.[40] The structure of the Zn-MOF-74 samples prepared in this study was verified through powder X-ray diffraction (PXRD), see Figure S3. The powder pattern of the as-synthesized structure showed a close correspondence with the simulated powder pattern derived from the single-crystal structure data, confirming its structure and high crystallinity. Notably, the PXRD patterns of Zn-MOF-74 revealed distinct diffraction maxima, with prominent ones observed at approximately 6.7 and 11.7° (2θ) with the remaining small but clear peaks at approximately 13.7, 18.1, 19.3, 21.5, 23.6, 24.7, 25.3, and 31.5°.

PXRD measurements for Cu-MOF-74 were performed at RT using a Panalytical X̂pert Cu Kα diffractometer with a 2θ range of 5−70°, a step size of 0.05°, and an exposure time of 10 s per step. This is a polycrystalline sample diffractometer with theta−theta geometry, a programmable slit, secondary graphite monochromator adjusted to copper radiation and fast solid-state PixCel detector adjusted to a 3.347° active length in 2θ (deg). Initially, the PXRD data were compared with the simulated patterns obtained from the crystallographic information files found at the Cambridge structural database. In addition, full-profile matching of the data was performed in order to discard the presence of secondary phases in the samples (Figure S4).

Thermogravimetric Analyses. MOF-74 samples were analyzed under synthetic air (25 mL/min) using a NETZSCH STA 449F3 DSC−TGA instrument for thermogravimetric analysis (TGA). The samples were placed in an alumina crucible (~25 mg of the sample) and then heated at 5 °C min^{-1} in the temperature range of 30−700 °C, see Figures S5 and S6.

Thermo-Diffraction Experiments. Temperature-dependent X-ray diffraction experiments were performed in a Bruker D8 Advance Bantec diffractometer (Cu Kα radiation), equipped with a variable-temperature stage HTK2000. The patterns were acquired in the 30 to 500 °C temperature range. Patterns were registered each 10 °C (2θ range = 5−40°, step size = 0.01°, exposure time = 0.5 s per step; Figures S5 and S6). Each pattern was fitted by a full-profile analysis without a structural model to extract the thermal evolution of the cell parameters during the compounds heating in an air atmosphere.

3DED Acquisition and Data Processing. All 3DED experiments have been performed on a Tecnai transmission electron microscope (Thermo Fisher, Eindhoven, the Netherlands) operated at 200 kV. The microscope was equipped with a CheeTah direct electron detector based on a Timepix chip (Amsterdam Scientific Instruments, Amsterdam, the Netherlands). Stage rotation speed was set at 3°/s while taking diffraction patterns at a rate of 12 fps, resulting in a step size of 0.261° between frames. A dose rate of approximately 28 e$^-$/nm^2 s was used during the tilt series (see Section S10 of the Supporting Information for the dose rate calculation). Every series took about 19 s, which results in a total dose of approximately 532 e$^-$/nm^2 for one series. Every acquisition was taken in less than 90 s, including the time required to center the crystal to the eucentric height. Consequently, the total illumination time of a particle throughout the entire experiment was less than 6 min. In order to avoid lens distortions as much as possible, we avoided high lens currents and used the same lens values during the entire experiment. This allows us to compare relative cell parameters of the same particle throughout the experiment.

This application of a fast acquisition and a significantly reduced electron dose served to minimize beam damage effectively. Heating of the sample was performed using a DENSsolutions (Delft, the Netherlands) Wildfire holder. A 5 nm amorphous carbon coating was applied to the back of the chip, using a Leica carbon coater, to avoid any charging of the chip.

The reconstruction of the reciprocal space sections and the extraction of the intensities of the reflections were done using Pets (version 2.0).[41] Frame scaling and distortion corrections based on the symmetry of the material were applied. Furthermore, trigonal symmetry was applied in all reconstructions. The intensities were integrated using the fit profile option. The structure was solved using SHELXL in Olex2,[42] along with a first kinematical refinement (with and without solvent masks). Further kinematical and dynamical refinements were performed using JANA2020 (version 04/10/2023).[43]

Only reflections where the intensity was higher than 3 × Sigma(I) were used during the refinements. Crystal structures and isosurface maps have been visualized using VESTA.[44] STEM−EDX maps were acquired using a probe-corrected Titan transmission electron microscope (Thermo Fisher, Eindhoven, the Netherlands) operated at 300 kV and equipped with a Super-X detector. The acquired EDX maps have been processed using Esprit by Bruker.

■ RESULTS AND DISCUSSION

MOF-74 has a well-known structure that consists of organic H$_4$dhtp (2,5-dihydroxyterephthalic acid) linkers and divalent transition metal centers (nodes). Combining these two building blocks adhering to a 5-c **bnn** net topology (see Figure S1) gives rise to one-dimensional edge shared transition metal-based octahedra further connected through the organic linkers to form a three-dimensional framework with large one-dimensional channels aligned along the [001] crystallographic direction, see Figures 2 and S2.
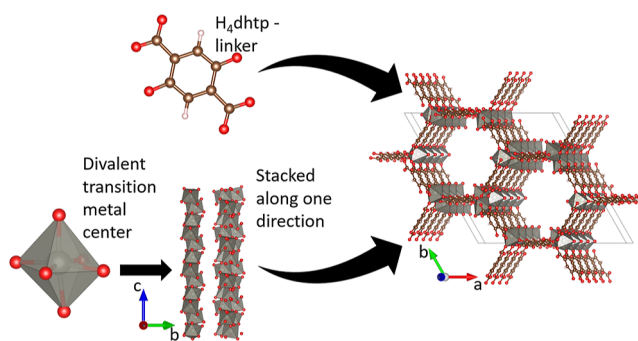

Figure 2. Building blocks of the MOF-74 structure. Red atoms represent O, brown ones C, and gray ones divalent transition metal atoms.

MOFs in general are very sensitive to the electron beam.[45,46] Customarily, the beam damage, caused by heating effects and radiolysis, to these materials is mitigated by using cryogenic conditions. However, since the activation process of MOFs occurs at raised temperatures, this is not an option for the current study. Therefore, beam damage was mitigated by reducing the total electron dose and increasing the speed of the acquisition. For this, we applied 3DED in continuous acquisition (cRED) using the CheeTah DED. The effectiveness of this mitigation is proven further on in the paper, where the structures solved from consecutively taken data sets are demonstrated to be unchanged. The activation procedure for Co-MOF-74, as used in literature,[47] involves discrete steps as illustrated in Figure S9. We applied a very similar process to activate the M-MOF-74 (M = Cu, Zn) samples. This involved heating the samples through discrete steps and concurrently capturing 3DED series after each step of the same particle to examine the activation process in-depth, see Figure S10.

Following a four-day solvent exchange in EtOH, the solution was drop-casted onto a heating chip. The chip's open design exposes the sample to an ultrahigh vacuum within the microscope, which is below 1.18 × 10^{-5} Pa. This value has high vacuum compared to the vacuum normally used for the activation of MOFs in standard conditions (from room pressure to 10^{-4} Pa) but below the vacuum conditions usually employed for activation in some micropore analysis (10^{-8} Pa).[23,47] Still, the vacuum applied in the sample holder is high enough to facilitate the removal of the EtOH within the pores.

The heating cycle used for both Zn-MOF-74 and Cu-MOF-74 is depicted in Figure S10. Both materials underwent an overnight heating process at 120 °C. We chose this temperature as it proved to be an activation temperature,[48] preserving the structural integrity without causing damage. A cRED data collection was performed at intervals marked as "post", resulting in a total of four data series acquired of each

Table 1. Structural Parameters, Olex2 Results, and Dynamical Refinement Jana Parameters and Results for Zn-MOF-74 and Cu-MOF-74[a]

	Zn-MOF-74					Cu-MOF-74	
	no SE*	post SE	post 120 °C	post 300 °C	post 350 °C	post SE	post 120 °C
max resolution (Å)	0.68	0.75	0.73	0.72	0.75	0.63	0.57
R_{int}(obs)	9.99	17.06	18.44	18.92	19.84	14.19	14.45
a (Å)	26.331 (1)	25.4215 (3)	26.7959 (2)	26.805 (8)	25.887 (7)	26.15 (8)	26.248 (7)
c (Å)	6.411 (2)	6.734 (3)	6.630 (7)	6.645 (3)	6.801 (3)	6.32 (3)	6.334 (2)
R_1(all) without a solvent mask (Olex2)	n.a	24.74	26.03	26.30	26.03	n.a	n.a
R_1(all) with a solvent mask (Olex2)	n.a	12.72	14.96	15.48	14.62	n.a	n.a
number of used reflections (Jana)	1668	1154	1276	1038	1057	454	417
R(obs) without a solvent mask (Jana)	12.64	13.11	14.65	13.59	12.34	13.93	14.49
wR(obs) without a solvent mask (Jana)	14.31	15.24	15.58	14.57	13.48	14.76	15.82
R(all) without a solvent mask (Jana)	14.95	13.92	16.73	14.68	14.07	15.18	15.26
wR(all) without a solvent mask (Jana)	14.44	15.28	15.72	14.61	13.77	14.82	15.84

[a]The space group $R\bar{3}$ was found for every dataset. The data for the nonsolvent exchanged (No SE) MOF was taken on a different particle, and this structure was solved and kinematically and dynamically refined in Jana. Other structures were solved and kinematically refined in Olex2 and subsequently dynamically refined in Jana.

particle (20 particles in total for Zn-MOF-74 and 25 for Cu-MOF-74). After the data acquisition, it was processed using the software Pets, for which the results are summarized in Table 1. Atomic coordinates, as well as ADPs (derived from structural solutions using Jana and Olex2, and refined with Jana, based on our own data), for all data sets can be found in the Supporting Information (Tables S2−S6). Distortion refinements and frame scaling with Laue class $\bar{3}$ were performed using the hexagonal lattice system. Outlier reflections were rejected following the procedure implemented in Pets and described in ref 49 using the threshold of $k = 1.5$. The "fit profile" option was employed for integrating the intensities of identified reflections.

In Table 1, we observe changes in the cell parameters upon heating, which are attributed to the pliability of the MOF to accommodate changes in the content of the pores. These variations are correlated with the thermal evolution of the cell parameters obtained from thermo-diffraction X-ray experiments, with an initial contraction of the framework due to the solvent release, followed by a slight structural thermal expansion, and ending in a fast contraction due to the structural collapse of Zn-MOF-74. Importantly, we observe that the resolution remains the same and there is only minimal change in Rint(obs), indicating that the beam damage, if any, is minimal. However, this does not preclude that the beam exposure could generate local defects within the MOF lattice without leading to its structural collapse.

Table 1 displays R-factors, indicators of the accuracy in structure solution and refinement. These factors, obtained through kinematical refinement using Olex2, are compared with and without incorporating a solvent mask. The solvent mask, when utilized, enables Olex2 to compute potential solvent-accessible voids while disregarding electron densities or electrostatic potentials within these voids. Notably, Table 1 reveals a substantial increase in the R-factor when the solvent mask is not applied. This difference suggests the persistence of electrostatic potentials within the pores even after completing the entire activation cycle, providing an initial indication of incomplete removal.

Next, we subjected the solved structures to dynamical refinements using JANA2020, therefore further reducing the dynamical effects in the structure refinement. While the kinematical refinements in Olex2 indicated the persistence of

electrostatic potentials within the pores, JANA2020 lacks an option for utilizing a solvent mask. Consequently, all components within the pores undergo refinement, elevating the R-factors. Table 1 presents the parameters derived from dynamical refinement, alongside the R-factors for the refined structures. The dynamical refinement led to a reduction in the R-factor (R_1 = 26.03, post 350 °C), down to 12.34 (R(obs), Post 350 °C), in comparison to the kinematically refined structures in Olex2 without the use of a solvent mask. Even with residual electrostatic potentials within the pores, R-factors <15 were achieved through dynamical refinement. These are similar to those obtained for other MOFs from 3DED data in literature.[50]

Figure 3 illustrates a comparison between the as-synthesized MOF structure, resolved through SCXRD under cryogenic
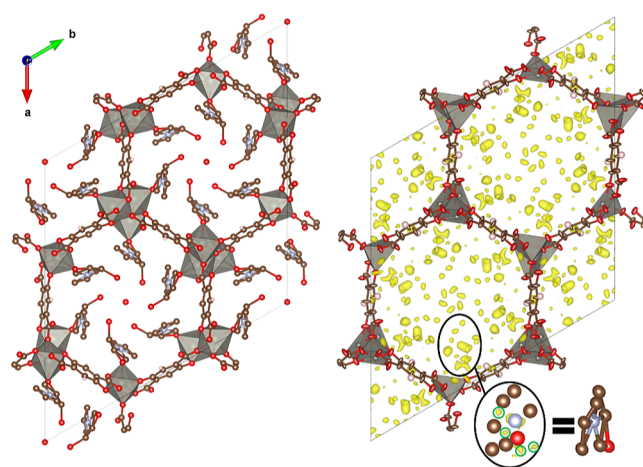

Figure 3. Left: Solved structure of as-synthesized Zn-MOF-74 based on XRD data taken at cryogenic temperatures. Right: Dynamically refined structure of the solvent-exchanged MOF, with the remaining electrostatic potentials (applied lower limit 0.095 eV/Å³ (2.3σ)) highlighted in yellow based on the difference Fourier calculation. The positions of the electrostatic potentials in the black oval agree with those of a DMF molecule. The atoms of the refined structure are displayed as their displacement ellipsoids. The green circles around some of the electrostatic potentials indicate unidentified atoms. Red atoms represent O, brown ones C, gray ones Zn, blue ones N, and pink ones H.

conditions, and the solvent-exchanged MOF structure obtained through our 3DED experiment before the heating cycle. The figure highlights residual electrostatic potentials, for which the positions match relatively close to DMF within the MOF pores. This comparison with the DMF molecule is only based on the positions of the residual electrostatic potentials since we were not able to refine the elemental compositions at these positions for reasons, explained below. This observation aligns with expectations from the literature that there is still DMF present after the solvent exchange step.[47] Moreover, the figure indicates the presence of additional unidentified electrostatic potentials, shown by the green circles.

The effectiveness of 3DED in discerning nuanced structural variations is underscored by this result. While there appears to be a distinction between the two structures, particularly evident in the octahedral arrangement, this discrepancy arises from the absence of the DMF O atom. As the weakest coordination bond in the octahedral coordination sphere around the metal, the DMF is predisposed to partial removal due to the ultrahigh-vacuum environment of the microscope and the solvent exchange process. Consequently, in Figure 3, it is represented solely as a lingering electrostatic potential, depicted as a red sphere overlapping on the magnified fragment.

The dynamically refined structures at all stages of the heating cycle are depicted in Figure 4. After heating the sample to 300 °C, open metal sites are visible, since there are no

Figure 4. Dynamically refined structures of Zn-MOF-74 at all the heating steps in the heating cycle, showing the remaining electrostatic potentials with values above 0.095 eV/Å³ (2.3σ). The atoms are displayed as their displacement ellipsoids. C atoms are displayed in brown, O atoms in red, and Zn-atoms in gray. The electrostatic potentials are displayed in yellow.

electrostatic potentials left inside the pores on reasonable bond distances from the Zn-atom of the metal node. This indicates the successful activation of the MOF. The MOF retains its crystalline framework even after elevating the temperature to 350 °C. Importantly, even though it is assumed in the literature that the pores are completely empty after heating in vacuum up to 300 °C, the 3DED data shows the presence of residual electrostatic potentials within the pores. Adding the ten largest remaining electrostatic potentials from Jana (see Section S9 in the Supporting Information) shows a clear decrease at each heating step. This confirms that atoms remain inside the pores after each step, although their quantity diminishes progressively.

This difference with literature can be due to the fact that 3DED is more sensitive than XRD to small molecules with low occupancies due to the stronger interaction between electrons and atoms or to the need for a higher coherence length in XRD. As the DMF molecules are only attached through a single coordination bond, they still have the freedom to rotate inside the pore, therefore reducing the coherence length of the atomic positions of the DMF atoms. Furthermore, the combination of the ultrahigh vacuum of the microscope and the solvent exchange cause a low occupancy at these crystallographic positions. The combination of these effects made it impossible for us to refine the elemental composition of the residual electrostatic potentials inside the pores. Unbound linkers, residual ethanol, and general atomic residue are alternative factors, aside from DMF, that can contribute to the presence of these lingering electrostatic potentials. The residual atoms within the pores will likely decrease the efficiency of the gas flow throughout the MOF.

Whereas the SCXRD data for MOFs is normally acquired at cryogenic temperatures, our measurements were conducted at room temperature and elevated temperatures where DMF should be in a "quasi" liquid form; however, the molecules that can be detected are those that are bonded to the MOF, giving them a more fixed position.

In Figure 5 (left), the metal octahedron of a dynamically refined structure (see Table 1) from a nonsolvent-exchanged Zn-MOF-74 is depicted, with the data acquired at room temperature. The influence of the ultrahigh-vacuum environment of the microscope is visible, leading to the splitting of the Zn position (from the original position to two symmetrically independent positions: Zn_1 and Zn_2. When DMF is removed due to the solvent exchange and the placement of the MOF into the ultrahigh vacuum of the microscope, the coordination of the Zn-atom will be reduced by 1. This will shorten all Zn–O bond lengths, therefore creating a different Zn position (Zn_2). The octahedral coordination will then become a pyramidal coordination as shown in Figure 6 (middle). This interpretation is corroborated when calculating the bond valence sums of both positions, as well as when refining the occupancies at each position, revealing a close correlation between the occupancies of Zn_2 and O_{DMF}.

Furthermore, we conducted an in situ study of the activation procedure for Cu-MOF-74, adhering to the identical heating cycle depicted in Figure S10. Our observations revealed that the sample underwent a transformation to a polycrystalline state after heating it to 300 °C, forming crystalline (as concluded from the observation of Kikuchi lines during the study) nanoparticles, as illustrated in Figure 6. This transition to nanostructured carbon underscores the considerable metal dependence on the thermal stability of the MOF. Such
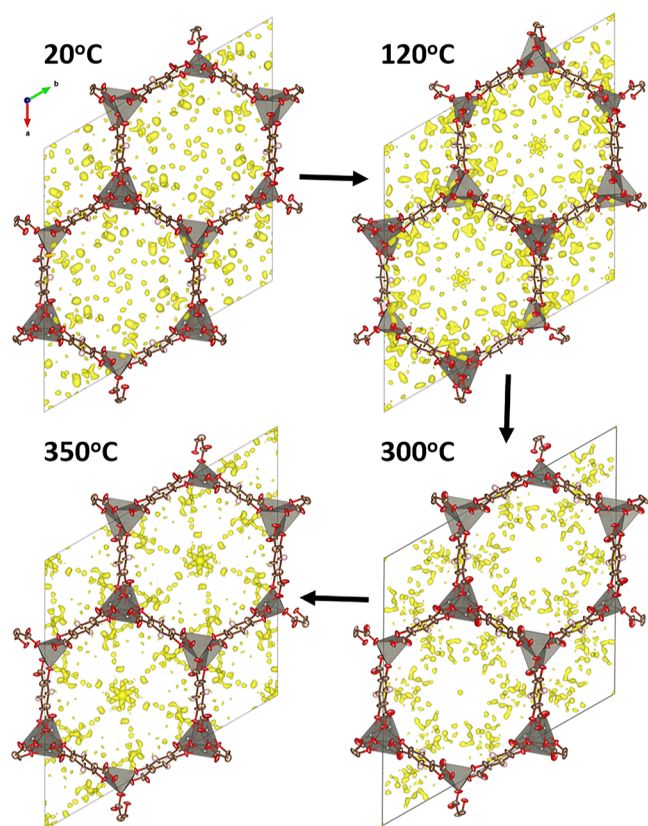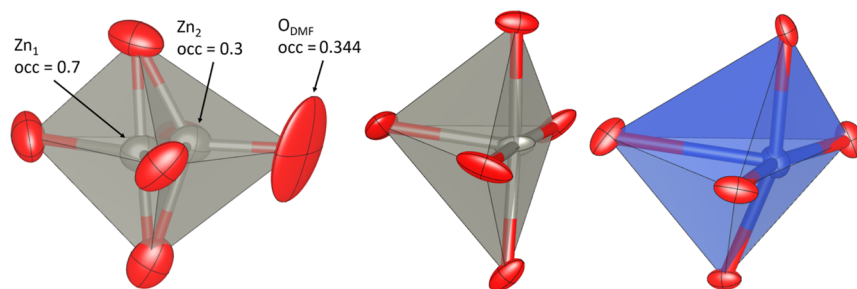
Figure 5. Left: Dynamically refined octahedron of a nonsolvent-exchanged Zn-MOF-74 crystal at room temperature. The refined occupancies of three atomic positions are indicated in the figure, abbreviated by "occ". Middle and Right: Pyramidal structure after heating to 120 °C for Zn- and Cu-MOF-74, respectively.
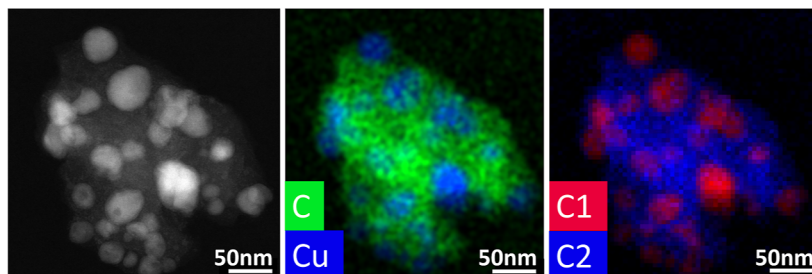

Figure 6. Left: HAADF-STEM image of the newly formed nanostructured carbon. Middle: STEM−EDX map of the nanostructured carbon, given in atomic percent. Right: Image showing the NMF components. Red denotes the first component (Cu nanoparticles) and blue the second component (C + O matrix), labeled C1 and C2, respectively. The third component (SiN-window) is not shown.

nanostructured carbons, often made through MOF-mediated synthesis, have potential as electrocatalysts.[51] The thermal dependence of the metal subunits into the MOF-74 family is further corroborated in the thermogravimetric and X-ray thermo-diffraction analyses Figures S5 and S6. In fact, the thermal evolution of the cell parameters for Cu-MOF-74 indicates a sudden collapse of the framework above 130 °C. To obtain the composition of the particles formed during the activation process (Cu vs CuO), we used non-negative matrix factorization (NMF) and neural networks using the Python package called Hyperspy, following the methodology outlined in ref 52 and as detailed in the Supporting Information, see Table S1. This indicates that the newly formed particles consist exclusively of Cu, while the surrounding carbon matrix incorporates all the C and O.

Given that the structure of Cu-MOF-74 retained crystallinity only up to 120 °C, the 3DED analysis focused only on two stages: the structure before heating at 20 °C (Post SE) and the structure after heating to 120 °C (Post 120 °C). Post-processing results for Cu-MOF-74 are given in Table 1. Atomic coordinates and anisotropic ADP parameters can be found in the Supporting Information Tables S7 and S8. For Cu-MOF-74, the structure was solved using Superflip and kinematically and dynamically refined in the software Jana2020. The dynamical refinement parameters for Cu-MOF-74 are also given in Table 1.

Figure 7 presents the dynamically refined structures for Post SE and Post 120 °C, overlaid with the remaining electrostatic potentials. The minimal presence of DMF and EtOH is discernible at the initiation of the heating cycle. Moreover, the heating cycle up to 120 °C appears to have almost no effect as there is very little DMF and EtOH present to be removed by this process. This suggests that the combination of solvent exchange with the ultrahigh-vacuum environment of the microscope is sufficient to generate open metal sites and
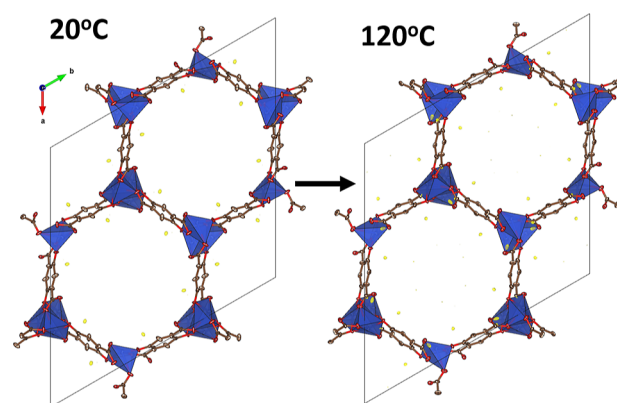

Figure 7. Dynamically refined structures of Cu-MOF-74 at Post SE (20 °C) and Post 120 °C, showing the remaining electrostatic potentials above 0.095 eV/Å^3 (2.3σ). The atoms are displayed as their displacement ellipsoids. C atoms are displayed in brown, O atoms in red, and Cu-atoms in blue. The electrostatic potentials are displayed in yellow.

activate Cu-MOF-74. One potential factor contributing to this phenomenon is the elevated Lewis acidity of Cu in comparison to that of Zn. This heightened Lewis acidity implies that the Cu−O coordination bond connecting the MOF structure and DMF will exhibit greater susceptibility to breakage.

Because there is no real change in the MOF pore content, we did not observe any big changes in the cell parameters of the MOF since it is already in a stable state after exposing the particle to the ultrahigh vacuum of the microscope. It is established in the literature that certain MOFs can be activated solely by exposure to vacuum, and the inclusion of a solvent exchange step further facilitates this effect.[53] The observed differences from Zn-MOF-74 can be explained by considering the Zn−O and Cu−O bonds. The Cu−O bond, characterized

by both a longer axial bond length (2.15−2.32 Å) and a lower binding energy compared to the Zn−O bond (1.876 Å)[54−56] (∼930 eV vs ∼1020 eV for Cu−O and Zn−O, respectively[57,58]), contributes to the different behaviors.

The difference in thermal stability between Zn-MOF-74 and Cu-MOF-74 arises from second-order Jahn−Teller distortions within the metal nodes.[59,60] For the activated structures refined in here, the corresponding polyhedra are shown in Figure 6 (middle and right). The pyramidal coordination is created by the removal of the oxygen that was part of the DMF due to the combined effect of solvent exchange and the ultrahigh vacuum in the microscope. The resultant second-order Jahn−Teller distortions induce a collapse of the linkers at lower temperatures than when these distortions are absent.

CONCLUSIONS

In this work, we were the first to study the activation process of a MOF using *in situ* electron microscopy. We closely monitored this process for M-MOF-74 (M = Cu, Zn) using *in situ* 3DED.

For Zn-MOF-74, heating to 300 °C successfully generated open metal sites on the metal nodes, indicative of successful activation. Surprisingly, heating to 350 °C did not render the MOF pores entirely empty, contrary to current literature reports. Remaining electrostatic potentials, representing residual atoms, were observed, which could potentially hinder gas flow during CO_2 absorption applications. Additionally, considerable changes in cell parameters were noted during the heating cycle, attributed to the inherent pliability of the MOF. The nonstatic positions of DMF atoms, coupled with factors like solvent exchange and ultrahigh vacuum, resulted in a low occupancy at the positions of the remaining electron potentials. Despite closely resembling DMF positions after overnight heating to 120 °C, these conditions prevented the refinement of the elemental composition of these potentials. In the other activation steps at 300 and 350 °C, the presence of the remaining potentials may be attributed to factors such as unbound linkers, residual ethanol, or atomic residue.

In contrast, in the case of Cu-MOF-74, open metal sites were already formed after solvent exchange and exposure to the ultrahigh vacuum, rendering further heating to 120 °C relatively ineffectual. This rapid activation is attributed to the longer and weaker Cu−O bond compared to the Zn−O bond, making the Cu−O bond between the MOF structure and the DMF more easily breakable. Additionally, the enhanced ease of activation can be ascribed to the greater Lewis acidity of Cu when compared to Zn. Moreover, for Cu-MOF-74, the material exhibited a special behavior, forming an amorphous carbon matrix with small Cu nanoparticles inside after heating to 300 °C. This difference in thermal stability is attributed to the higher Lewis acidity, as well as second-order Jahn−Teller distortions within the metal octahedra of Cu-MOF.

All in all, these findings shed light on the diverse activation dynamics and behaviors exhibited by different metal-based MOFs. We believe that these new insights into the activation of MOF-74 can provide a better understanding that might prove valuable for the MOF applications and design in general, as well as illustrating the potential of *in situ* 3DED to study these materials.

ASSOCIATED CONTENT

ⓢ Supporting Information

The Supporting Information is available free of charge at https://pubs.acs.org/doi/10.1021/acs.chemmater.4c01153.

> Detailed description of the MOF-74 structure, PXRD measurements, TGA measurements, NMF quantification, TEM images of M-MOF-74 (M = Cu, Zn), discrete heating steps of Co-MOF-74 and detailed description of the heating process, heating curve used during the *in situ* experiment, atomic coordinates and anisotropic ADP parameters for all data sets used in the main text, and remaining electrostatic potentials given by Jana and Dose rate calculation (PDF)

AUTHOR INFORMATION

Corresponding Author

Joke Hadermann − *EMAT, Department of Physics, University of Antwerp, 2020 Antwerp, Belgium;* ⓞ orcid.org/0000-0002-1756-2566; Email: joke.hadermann@uantwerpen.be

Authors

Matthias Quintelier − *EMAT, Department of Physics, University of Antwerp, 2020 Antwerp, Belgium;* ⓞ orcid.org/0000-0003-0206-0261

Amirhossein Hajizadeh − *EMAT, Department of Physics, University of Antwerp, 2020 Antwerp, Belgium*

Alexander Zintler − *EMAT, Department of Physics, University of Antwerp, 2020 Antwerp, Belgium*

Bruna F. Gonçalves − *BCMaterials, Basque Center for Materials, Applications and Nanostructures, 48940 Leioa, Spain;* ⓞ orcid.org/0000-0003-0633-9251

Roberto Fernández de Luis − *BCMaterials, Basque Center for Materials, Applications and Nanostructures, 48940 Leioa, Spain;* ⓞ orcid.org/0000-0002-8924-230X

Leili Esrafili Dizaji − *Faculty of Applied Engineering, iPRACS, University of Antwerp, 2020 Antwerp, Belgium*

Christophe M. L. Vande Velde − *Faculty of Applied Engineering, iPRACS, University of Antwerp, 2020 Antwerp, Belgium;* ⓞ orcid.org/0000-0002-5007-2315

Stefan Wuttke − *BCMaterials, Basque Center for Materials, Applications and Nanostructures, 48940 Leioa, Spain; Ikerbasque, Basque Foundation for Science, Bilbao 48009, Spain;* ⓞ orcid.org/0000-0002-6344-5782

Complete contact information is available at:
https://pubs.acs.org/10.1021/acs.chemmater.4c01153

Author Contributions

Conceptualization, M.Q. and J.H.; methodology, M.Q. and J.H.; data processing, M.Q., A.H., and A.Z.; formal analysis, all authors; material synthesis, R.L., L.E.D.; investigation, M.Q.; resources, J.H.; writing—original draft preparation, M.Q., S.W., and J.H.; writing—review and editing, all authors. All authors have read and agreed to the published version of the manuscript.

Notes

The authors declare no competing financial interest.

■ ABBREVIATIONS

TEM, transmission electron microscope/microscopy; 3DED, three-dimensional electron diffraction; XRD, X-ray diffraction; SCXRD, single-crystal X-ray diffraction; PXRD, powder X-ray diffraction; cRED, continuous rotation electron diffraction; SE, solvent exchange; MOF, metal-organic framework; DMF, *N,N*-dimethylformamide; EtOH, ethanol; HAADF-STEM, high-angle annular dark field scanning transmission electron microscopy; NMF, non-negative matrix factorization

■ REFERENCES

(1) Freund, R.; Canossa, S.; Cohen, S. M.; Yan, W.; Deng, H.; Guillerm, V.; Eddaoudi, M.; Madden, D. G.; Fairen-Jimenez, D.; Lyu, H.; Macreadie, L. K.; Ji, Z.; Zhang, Y.; Wang, B.; Haase, F.; Woll, C.; Zaremba, O.; Andreo, J.; Wuttke, S.; Diercks, C. S. *Angew. Chem. Int. Ed.* **2021**, *60*, 23946.

(2) Furukawa, H.; Cordova, K. E.; O'Keeffe, M.; Yaghi, O. M. The chemistry and applications of metal-organic frameworks. *Science* **2013**, *341* (6149), 1230444.

(3) Ji, Z.; Wang, H.; Canossa, S.; Wuttke, S.; Yaghi, O. M. Pore Chemistry of Metal−Organic Frameworks. *Adv. Funct. Mater.* **2020**, *30* (41), 2000238.

(4) Sumida, K.; Rogow, D. L.; Mason, J. A.; McDonald, T. M.; Bloch, E. D.; Herm, Z. R.; Bae, T. H.; Long, J. R. Carbon dioxide capture in metal-organic frameworks. *Chem. Rev.* **2012**, *112* (2), 724−781.

(5) Sanz, R.; Martínez, F.; Orcajo, G.; Wojtas, L.; Briones, D. Synthesis of a honeycomb-like Cu-based metal-organic framework and its carbon dioxide adsorption behaviour. *Dalton Trans.* **2013**, *42* (7), 2392−2398.

(6) Freund, R.; Zaremba, O.; Arnauts, G.; Ameloot, R.; Skorupskii, G.; Dincă, M.; Bavykina, A.; Gascon, J.; Ejsmont, A.; Goscianska, J.; et al. The Current Status of MOF and COF Applications. *Angew. Chem., Int. Ed.* **2021**, *60* (45), 23975−24001.

(7) McDonald, T. M.; Lee, W. R.; Mason, J. A.; Wiers, B. M.; Hong, C. S.; Long, J. R. Capture of carbon dioxide from air and flue gas in the alkylamine-appended metal-organic framework mmen-Mg 2-(dobpdc). *J. Am. Chem. Soc.* **2012**, *134* (16), 7056−7065.

(8) McDonald, T. M.; Mason, J. A.; Kong, X.; Bloch, E. D.; Gygi, D.; Dani, A.; Crocellà, V.; Giordanino, F.; Odoh, S. O.; Drisdell, W. S.; et al. Cooperative insertion of CO_2 in diamine-appended metal-organic frameworks. *Nature* **2015**, *519* (7543), 303−308.

(9) Cho, H. Y.; Yang, D. A.; Kim, J.; Jeong, S. Y.; Ahn, W. S. CO_2 adsorption and catalytic application of Co-MOF-74 synthesized by microwave heating. *Catal. Today* **2012**, *185*, 35−40.

(10) Valenzano, L.; Civalleri, B.; Chavan, S.; Palomino, G. T.; Areán, C. O.; Bordiga, S. Computational and experimental studies on the adsorption of CO, N_2, and CO_2 on Mg-MOF-74. *J. Phys. Chem. C* **2010**, *114* (25), 11185−11191.

(11) Britt, D.; Furukawa, H.; Wang, B.; Glover, T. G.; Yaghi, O. M. Highly efficient separation of carbon dioxide by a metal-organic framework replete with open metal sites. *Proc. Natl. Acad. Sci. U.S.A.* **2009**, *106* (49), 20637−20640.

(12) Millward, A. R.; Yaghi, O. M. Metal-organic frameworks with exceptionally high capacity for storage of carbon dioxide at room temperature. *J. Am. Chem. Soc.* **2005**, *127* (51), 17998−17999.

(13) Choi, I.; Jung, Y. E.; Yoo, S. J.; Kim, J. Y.; Kim, H. J.; Lee, C. Y.; Jang, J. H. Facile synthesis of M-MOF-74 (M = Co, Ni, Zn) and its application as an electrocatalyst for electrochemical CO_2 conversion and H_2 production. *J. Electrochem. Sci. Technol.* **2017**, *8* (1), 61−68.

(14) Choe, J. H.; Kim, H.; Hong, C. S. MOF-74 type variants for CO_2 capture. *Mater. Chem. Front.* **2021**, *5* (14), 5172−5185.

(15) Trickett, C. A.; Helal, A.; Al-Maythalony, B. A.; Yamani, Z. H.; Cordova, K. E.; Yaghi, O. M. The chemistry of metal-organic frameworks for CO2 capture, regeneration and conversion. *Nat. Rev. Mater.* **2017**, *2* (8), 17045.

(16) Chen, S.; Li, X.; Duan, J.; Fu, Y.; Wang, Z.; Zhu, M.; Li, N. Investigation of highly efficient adsorbent based on Ni-MOF-74 in the separation of CO_2 from natural gas. *Chem. Eng. J.* **2021**, *419*, 129653.

(17) Bhadra, B. N.; Yoo, D. K.; Jhung, S. H. Carbon-derived from metal-organic framework MOF-74: A remarkable adsorbent to remove a wide range of contaminants of emerging concern from water. *Appl. Surf. Sci.* **2020**, *504*, 144348.

(18) Strauss, I.; Mundstock, A.; Treger, M.; Lange, K.; Hwang, S.; Chmelik, C.; Rusch, P.; Bigall, N. C.; Pichler, T.; Shiozawa, H.; et al. Metal-Organic Framework Co-MOF-74-Based Host-Guest Composites for Resistive Gas Sensing. *ACS Appl. Mater. Interfaces* **2019**, *11* (15), 14175−14181.

(19) Schnabel, J.; Ettlinger, R.; Bunzen, H. Zn-MOF-74 as pH-Responsive Drug-Delivery System of Arsenic Trioxide. *ChemNanoMat* **2020**, *6* (8), 1229−1236.

(20) Howarth, A. J.; Peters, A. W.; Vermeulen, N. A.; Wang, T. C.; Hupp, J. T.; Farha, O. K. Best practices for the synthesis, activation, and characterization of metal−organic frameworks. *Chem. Mater.* **2017**, *29* (1), 26−39.

(21) Gropp, C.; Canossa, S.; Wuttke, S.; Gándara, F.; Li, Q.; Gagliardi, L.; Yaghi, O. M. Standard Practices of Reticular Chemistry. *ACS Cent. Sci.* **2020**, *6* (8), 1255−1273.

(22) Mondloch, J. E.; Karagiaridi, O.; Farha, O. K.; Hupp, J. T. Activation of metal-organic framework materials. *CrystEngComm* **2013**, *15* (45), 9258−9264.

(23) Otun, K. O. Temperature-controlled activation and characterization of iron-based metal-organic frameworks. *Inorg. Chim. Acta* **2020**, *507*, 119563.

(24) Akeremale, O. K.; Ore, O. T.; Bayode, A. A.; Badamasi, H.; Adedeji Olusola, J.; Durodola, S. S. Synthesis, characterization, and activation of metal organic frameworks (MOFs) for the removal of emerging organic contaminants through the adsorption-oriented process: A review. *Results Chem.* **2023**, *5*, 100866.

(25) Díaz-García, M.; Mayoral, A.; Díaz, I.; Sánchez-Sánchez, M. Nanoscaled M-MOF-74 materials prepared at room temperature. *Cryst. Growth Des.* **2014**, *14* (5), 2479−2487.

(26) Gemmi, M.; Mugnaioli, E.; Gorelik, T. E.; Kolb, U.; Palatinus, L.; Boullay, P.; Hovmöller, S.; Abrahams, J. P. 3D electron diffraction: The nanocrystallography revolution. *ACS Cent. Sci.* **2019**, *5* (8), 1315−1329.

(27) Gemmi, M.; Lanza, A. 3D electron diffraction techniques. *Acta Crystallogr., Sect. B: Struct. Sci., Cryst. Eng. Mater.* **2019**, *75*, 495.

(28) Huang, Z.; Grape, E. S.; Li, J.; Inge, A. K.; Zou, X. 3D electron diffraction as an important technique for structure elucidation of metal-organic frameworks and covalent organic frameworks. *Coord. Chem. Rev.* **2021**, *427*, 213583.

(29) Leubner, S.; Zhao, H.; Van Velthoven, N.; Henrion, M.; Reinsch, H.; De Vos, D. E.; Kolb, U.; Stock, N. Expanding the Variety

of Zirconium-based Inorganic Building Units for Metal−Organic Frameworks. *Angew. Chem., Int. Ed.* **2019**, *58* (32), 10995−11000.

(30) Coates, L.; Cao, H. B.; Chakoumakos, B. C.; Frontzek, M. D.; Hoffmann, C.; Kovalevsky, A. Y.; Liu, Y.; Meilleur, F.; dos Santos, A. M.; Myles, D. A. A.; et al. A suite-level review of the neutron single-crystal diffraction instruments at Oak Ridge National Laboratory. *Rev. Sci. Instrum.* **2018**, *89* (9), 092802.

(31) Marchetti, D.; Pedrini, A.; Massera, C.; Faye Diouf, M. D.; Jandl, C.; Steinfeld, G.; Gemmi, M. 3D electron diffraction analysis of a novel, mechanochemically synthesized supramolecular organic framework based on tetrakis-4-(4- pyridyl)phenylmethane. *Acta Crystallogr., Sect. B: Struct. Sci., Cryst. Eng. Mater.* **2023**, *79*, 432−436.

(32) Ge, M.; Yang, T.; Xu, H.; Zou, X.; Huang, Z. Direct Location of Organic Molecules in Framework Materials by Three-Dimensional Electron Diffraction. *J. Am. Chem. Soc.* **2022**, *144* (33), 15165−15174.

(33) Kolb, U.; Krysiak, Y.; Plana-Ruiz, S. Automated electron diffraction tomography - Development and applications. *Acta Crystallogr., Sect. B: Struct. Sci., Cryst. Eng. Mater.* **2019**, *75*, 463−474.

(34) Cichocka, M. O.; Ångström, J.; Wang, B.; Zou, X.; Smeets, S. High-throughput continuous rotation electron diffraction data acquisition via software automation. *J. Appl. Crystallogr.* **2018**, *51* (6), 1652−1661.

(35) Gemmi, M.; Mugnaioli, E.; Gorelik, T. E.; Kolb, U.; Palatinus, L.; Boullay, P.; Hovmöller, S.; Abrahams, J. P. 3D electron diffraction: The nanocrystallography revolution. *ACS Cent. Sci.* **2019**, *5* (8), 1315−1329.

(36) Palatinus, L.; et al. Hydrogen positions in single nanocrystals revealed by electron diffraction. http://science.sciencemag.org/.

(37) Poppe, R.; Vandemeulebroucke, D.; Neder, R. B.; Hadermann, J.; Meshi, L. Quantitative analysis of diffuse electron scattering in the lithium-ion battery cathode material Li1.2Ni0.13Mn0.54Co0.13O2. *IUCrJ* **2022**, *9* (5), 695−704.

(38) Quintelier, M.; Perkisas, T.; Poppe, R.; Batuk, M.; Hendrickx, M.; Hadermann, J. Determination of spinel content in cycled Li1.2Ni0.13Mn0.54Co0.13O2 using three-dimensional electron diffraction and precession electron diffraction. *Symmetry* **2021**, *13* (11), 1989.

(39) Liao, Y.; Zhang, L.; Weston, M. H.; Morris, W.; Hupp, J. T.; Farha, O. K. Tuning ethylene gas adsorption via metal node modulation: Cu-MOF-74 for a high ethylene deliverable capacity. *Chemical Communications* **2017**, *53*, 9376−9379.

(40) Rosi, N. L.; Kim, J.; Eddaoudi, M.; Chen, B.; O'Keeffe, M.; Yaghi, O. M. Rod packings and metal-organic frameworks constructed from rod-shaped secondary building units. *J. Am. Chem. Soc.* **2005**, *127* (5), 1504−1518.

(41) Palatinus, L.; Brázda, P.; Jelínek, M.; Hrdá, J.; Steciuk, G.; Klementová, M. Specifics of the data processing of precession electron diffraction tomography data and their implementation in the program PETS2.0. *Acta Crystallogr., Sect. B: Struct. Sci., Cryst. Eng. Mater.* **2019**, *75*, 512−522.

(42) Dolomanov, O. V.; Bourhis, L. J.; Gildea, R. J.; Howard, J. A. K.; Puschmann, H. OLEX2: A complete structure solution, refinement and analysis program. *J. Appl. Crystallogr.* **2009**, *42* (2), 339−341.

(43) Petrícek, V.; Dušek, M.; Palatinus, L. Crystallographic computing system JANA2006: General features. *Z. Krystallog.* **2014**, *229* (5), 345−352.

(44) Momma, K.; Izumi, F. VESTA: A three-dimensional visualization system for electronic and structural analysis. *J. Appl. Crystallogr.* **2008**, *41* (3), 653−658.

(45) Chen, Q.; Dwyer, C.; Sheng, G.; Zhu, C.; Li, X.; Zheng, C.; Zhu, Y. Imaging Beam-Sensitive Materials by Electron Microscopy. *Adv. Mater.* **2020**, *32* (16), 1907619.

(46) Wiktor, C.; Meledina, M.; Turner, S.; Lebedev, O. I.; Fischer, R. A. Transmission electron microscopy on metal-organic frameworks-a review. *J. Mater. Chem. A* **2017**, *5* (29), 14969−14989.

(47) Liang, X.; Wang, P.; Li, C.; Yuan, M.; Shi, Q.; Dong, J. The activation of Co-MOF-74 with open metal sites and their

corresponding CO/N_2 adsorptive separation performance. *Microporous Mesoporous Mater.* **2021**, *320*, 111109.

(48) Wright, K. R.; Nath, K.; Matzger, A. J. Superior Metal-Organic Framework Activation with Dimethyl Ether. *Angew. Chem., Int. Ed.* **2022**, *61* (52), No. e202213190.

(49) Khouchen, M.; Klar, P. B.; Chintakindi, H.; Suresh, A.; Palatinus, L. Optimal estimated standard uncertainties of reflection intensities for kinematical refinement from 3D electron diffraction data. *Acta Crystallogr., Sect. A: Found. Adv.* **2023**, *79*, 427−439.

(50) Samperisi, L.; Zou, X.; Huang, Z. How to get maximum structure information from anisotropic displacement parameters obtained by three-dimensional electron diffraction: an experimental study on metal-organic frameworks. *IUCrJ* **2022**, *9*, 480−491.

(51) Oar-Arteta, L.; Wezendonk, T.; Sun, X.; Kapteijn, F.; Gascon, J. Metal organic frameworks as precursors for the manufacture of advanced catalytic materials. *Mater. Chem. Front.* **2017**, *1* (9), 1709−1745.

(52) Rossouw, D.; Burdet, P.; de la Peña, F.; Ducati, C.; Knappett, B. R.; Wheatley, A. E. H.; Midgley, P. A. Multicomponent Signal Unmixing from Nanoheterostructures: Overcoming the Traditional Challenges of Nanoscale X-ray Analysis via Machine Learning. *Nano Lett.* **2015**, *15* (4), 2716−2720.

(53) Zhang, X.; Chen, Z.; Liu, X.; Hanna, S. L.; Wang, X.; Taheri-Ledari, R.; Maleki, A.; Li, P.; Farha, O. K. A historical overview of the activation and porosity of metal-organic frameworks. *Chem. Soc. Rev.* **2020**, *49* (20), 7406−7427.

(54) Huang, C. H.; Jan, Y. L.; Chuang, W. J.; Lu, P. T. Investigation of approaches to control the compositions of Zn(Se,OH) buffers prepared by chemical bath deposition process for Cu(In,Ga)Se2 (CIGS) solar cells. *Crystals* **2018**, *8* (9), 343.

(55) Ali, A.; Hussain, S.; Bhatti, H. S.; Shabbir, B. Study of structural, electronic, and conducting properties of $Cu_{2−x}Mn_xO$ ($0 \leq x \leq 0.07$) system. *Results Phys.* **2021**, *25*, 104224.

(56) Persson, I.; Lundberg, D.; Bajnóczi, E. ·. G.; Klementiev, K.; Just, J.; Sigfridsson Clauss, K. G. V. EXAFS Study on the Coordination Chemistry of the Solvated Copper(II) Ion in a Series of Oxygen Donor Solvents. *Inorg. Chem.* **2020**, *59* (14), 9538−9550.

(57) Sung, M. M.; Kim, Y. Self-assembled monolayers of alkanethiols on clean copper surfaces. *Bull. Korean Chem. Soc.* **2001**, *22* (7), 748−752.

(58) Kamarulzaman, N.; Kasim, M. F.; Chayed, N. F. Elucidation of the highest valence band and lowest conduction band shifts using XPS for ZnO and $Zn_{0.99}Cu_{0.01}O$ band gap changes. *Results Phys.* **2016**, *6*, 217−230.

(59) Flores, J. G.; Aguilar-Pliego, J.; Martin-Guaregua, N.; Ibarra, I. A.; Sanchez-Sanchez, M. Room-temperature prepared bimetallic nanocrystalline MOF-74 as catalysts in the aerobic oxidation of cyclohexene. *Catal. Today* **2022**, *394−396*, 295−303.

(60) Molina, M. A.; Manjón-Sanz, A.; Sánchez-Sánchez, M. On the contribution of Pair Distribution Function (PDF) to the characterization of nanocrystalline MOFs: The case of M-MOF-74. *Microporous Mesoporous Mater.* **2021**, *319*, 110973.